Title

Two-Dimensional Electronic–Vibrational Spectroscopy of Coupled Molecular Complexes: A Near-Analytical Approach

Journal

The Journal of Physical Chemistry Letters, 10(9)

ISSN

1948-7185

Authors

Bhattacharyya, Pallavi
Fleming, Graham R

Publication Date

2019-05-02

DOI

10.1021/acs.jpclett.9b00588

Peer reviewed

Two-Dimensional Electronic-Vibrational Spectroscopy of Coupled Molecular Complexes: A Near Analytical Approach

Pallavi Bhattacharyya[†,‡,¶] and Graham R. Fleming[*,†,‡,¶]

†*Department of Chemistry, University of California, Berkeley 94720, USA*

‡*Molecular Biophysics and Integrated Bioimaging Division, Lawrence Berkeley National Lab, Berkeley, California 94720, USA*

¶*Kavli Energy Nanosciences Institute at Berkeley, Berkeley, California 94720, USA*

E-mail: grfleming@lbl.gov

Abstract

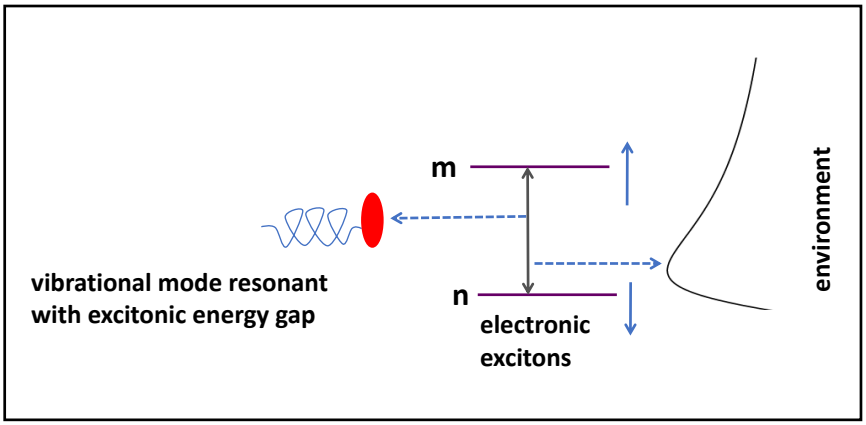

This work presents theoretical calculations of the two-dimensional electronic vibrational (2DEV) spectrum of a vibronically coupled molecular dimer using a near-analytical method. In strongly coupled dimers, where the IR mode is resonant with the electronic energy gap between the excitons, multiple infrared transitions become allowed that are forbidden in weakly coupled systems that have a non-resonant IR mode.

This formalism enables the coherences and population contributions to be explored separately, and allows efficient calculation of relaxation rates between the vibronic states. At short times we find strong contributions of vibronic coherences to the 2DEV spectra. They decay fairly rapidly giving rise to strong population signals. Although the interpretation of 2DEV spectra is considerably more complex than for weakly coupled systems, the richness of the spectra and the necessity to consider both visible and infrared transition moments suggest that such analysis will be very valuable in characterizing the role of vibronic effects in ultrafast molecular dynamics.

Two Dimensional Electronic Vibrational (2DEV) spectroscopy is a newly developing nonlinear four-wave mixing technique, where two UV-vis pulses interact with the system of interest, followed by an IR pulse and eventually the system emits the signal IR pulse.[1–6] Two Dimensional Vibrational Electronic (2DVE) spectroscopy is a complimentary method in which two IR pulses initially interact with the system, followed by an UV-vis pulse and the subsequent emission of a UV-vis pulse by the system is detected.[7] Their well-established counterparts, 2DES[8–10] (Two Dimensional Electronic Spectroscopy) and 2DIR[11–13] (Two Dimensional Infrared Spectroscopy) aim at investigating the temporal evolution of electronic excitation and the consequent effects on dynamics, and the structural evolution in the ground state, probed through IR frequencies, respectively. 2DEV spectroscopy aims at bridging the gap between the electronic and vibrational regimes, to elucidate how photo-excited electronic excitation dynamics and structure, probed through vibrations, are inter-related. This is specifically relevant for systems in condensed phase such as the photosynthetic light harvesting complexes. Here, the chromophores, despite identical structures and hence, energies, if isolated, have an energy gradient, since the structures of the chromophores are modulated and shaped by their mutual interactions and respective local environments. This, in turn, increases the absorption bandwidth as well as creating an energy gradient for excitation energy from the absorption site to the reaction center.

The observation of long lived quantum beating, in a photosystem with an elaborate en-

vironment, is a subject of persistent intrigue.[14] An example of such a complex system is the photosynthetic FMO complex of the green sulfur bacteria with an oscillation lifetime of 660 fs at 77 K.[15] The initial interpretation attributed these persistent quantum beatings to a coherent wave-like transfer of electronic excitation among the optically excited eigenstates. However, the presence of a complex environment should cause rapid decoherence, leading to incoherent, Forster-like hopping of electronic excitation after a very short time among the chromophores. An alternative conjecture attributes the persistence of such coherent oscillations to long-range fluctuations of the protein scaffold.[16] Jonas and coworkers suggested that the long-lived oscillations stem from vibrational wavepackets on the ground electronic state, a manifestation of the delocalized, anti-correlated component of pigment vibrations that drive nonadiabatic electronic energy transport.[17] Another rationale proposes that the long oscillation lifetimes arise due to Vibrationally Assisted Electronic Energy Transfer (VA-EET).[18–28] Here, the nuclear degrees of freedom are hypothesized to contribute a discrete, sharp vibrational/nuclear mode that is resonant/quasi- resonant with a pair of electronic excitons. A back and forth coherent transfer of excitation between the excitons and such a discrete mode could act like a field, driving Rabi-like oscillations, causing the excitonic coherences to be retained longer than the expected decoherence timescale. However, recent studies report that for modes with fairly small Huang Rhys factors, such electronic-vibrational quantum mixtures, despite contributing to the long-lived spectral beating, do not play a major role in electronic energy transport. It is, thus, important to appreciate that it is often non-trivial to directly relate the experimental spectra to the system dynamics.[29] It is imperative, then, to model these different phenomena theoretically with a consistent model for both spectral and population dynamics and use the information obtained to explain and understand the experimental findings. To this end, we use 2DEV (2 Dimensional Electronic Vibrational) spectroscopy, to investigate how the excitation energy evolves temporally and spatially. Theoretical simulations are essential to enable an understanding of how the system dynamics result in specific signatures in the 2DEV spectra. For mechanistic insight, we propose a

computationally efficient approach that is essentially analytical in calculating decoherence to evaluate 2DEV spectra of coupled dimers, using nonlinear response functions. We expect that the features we obtain will also appear in more rigorous and exact numerical simulations.

We consider a dimer, with an IR mode of angular frequency Ω ($\Omega = \Omega_A = \Omega_B, \hbar = 1$), local to each of the monomers (labeled A and B, respectively), as the system of interest. The IR modes on A and B are considered to have zero coupling with the other monomer. The electronic coupling between A and B is given as $\langle A \mid H \mid B\rangle = \langle B \mid H \mid A\rangle = J$. The IR mode has a frequency that is resonant with the energy gap between the electronic excitons, formed from A and B, resulting in a strongly coupled dimeric system. The site basis, therefore, should reflect information about both the electronic and vibrational degrees of freedom and is given as $\mid X v_\alpha^A v_\beta^B\rangle$. Here, $X \in \{g, A, B\}$ labels the electronic state, where g denotes both A and B are in their respective ground states, A indicates that only A is electronically excited whereas B denotes that only B is electronically excited. Doubly-excited electronic states are not considered, as they are not accessible in 2DEV spectroscopy. The superscript on v labels if the vibrational mode is local to A or B and $\{\alpha, \beta\} \in \{g0, g1, e0^{'}, e1^{'}\}$, where g and e denote if the monomer is in the ground or first excited electronic state, respectively. 0 and 1 are the ground and first excited vibrational states on g, whereas $0^{'}$ and $1^{'}$ label the ground and first excited vibrational states on e. For initial calculations, in the site basis, we approximate that the electronic wavefunctions are independent of the nuclear wavefunctions, therefore, $\mid X v_\alpha^A v_\beta^B\rangle \approx \mid X\rangle \otimes \mid v_\alpha^A\rangle \otimes \mid v_\beta^B\rangle$. The Huang Rhys factor, σ, describes the vibrational overlap between the nuclear wavefunctions on the ground and excited electronic states, for a given monomer: $\langle v_{g0}^A \mid v_{e0'}^A\rangle = e^{-\sigma/2}$; $\langle v_{g0}^A \mid v_{e1'}^A\rangle = \sqrt{\sigma} e^{-\sigma/2}$; $\langle v_{e0'}^A \mid v_{g1}^A\rangle \approx -\sqrt{\sigma} e^{-\sigma/2}$;$\langle v_{g1}^A \mid v_{e1'}^A\rangle = (1-\sigma) e^{-\sigma/2}$. In these expressions, we ignore frequency changes in the modes between ground and excited states. This is a reasonable approximation for the chlorophyll molecules that comprise green plant antennae.

The 2DEV spectra for coupled dimers, when described by nonlinear response functions, have contributions from the Ground State Bleaching (GSB), Excited State Emission (ESE)

and Excited State Absorption (ESA) pathways (see Figure 1). It is important to note that the ground and the excited electronic states are coupled only radiatively. For the GSB pathway, we work with the system Hamiltonian, $H_{sys,g}$, in the ground electronic state manifold, described by the basis states $\mid gv_{g0}^{A}v_{g0}^{B}\rangle$, $\mid gv_{g0}^{A}v_{g1}^{B}\rangle$ and $\mid gv_{g1}^{A}v_{g0}^{B}\rangle$, respectively. The state $\mid gv_{g0}^{A}v_{g0}^{B}\rangle$ is considered to have the zero of energy. $H_{sys,g}$ is, therefore, given as:

$$H_{sys,g} = \begin{pmatrix} 0 & 0 & 0 \\ 0 & \Omega & 0 \\ 0 & 0 & \Omega \end{pmatrix}. \tag{1}$$

The ESA and ESE pathways, on the other hand, are described by the system Hamiltonian in the electronic excited state manifold, $H_{sys,ex}$, formed by the basis states $\mid Av_{e0'}^{A}v_{g0}^{B}\rangle$, $\mid Av_{e1'}^{A}v_{g0}^{B}\rangle$, $\mid Av_{e0'}^{A}v_{g1}^{B}\rangle$, $\mid Bv_{g0}^{A}v_{e0'}^{B}\rangle$, $\mid Bv_{g0}^{A}v_{e1'}^{B}\rangle$ and $\mid Bv_{g1}^{A}v_{e0'}^{B}\rangle$ (the site states are labeled as I, II, III, IV, V and VI, respectively), and given as:

$$H_{sys,ex} = \begin{pmatrix} E_A & 0 & 0 & Je^{-\sigma} & J\sqrt{\sigma}e^{-\sigma} & -J\sqrt{\sigma}e^{-\sigma} \\ 0 & E_A+\Omega' & 0 & J\sqrt{\sigma}e^{-\sigma} & J\sigma e^{-\sigma} & J(1-\sigma)e^{-\sigma} \\ 0 & 0 & E_A+\Omega & -J\sqrt{\sigma}e^{-\sigma} & J(1-\sigma)e^{-\sigma} & J\sigma e^{-\sigma} \\ Je^{-\sigma} & J\sqrt{\sigma}e^{-\sigma} & -J\sqrt{\sigma}e^{-\sigma} & E_B & 0 & 0 \\ J\sqrt{\sigma}e^{-\sigma} & J\sigma e^{-\sigma} & J(1-\sigma)e^{-\sigma} & 0 & E_B+\Omega' & 0 \\ -J\sqrt{\sigma}e^{-\sigma} & J(1-\sigma)e^{-\sigma} & J\sigma e^{-\sigma} & 0 & 0 & E_B+\Omega \end{pmatrix}. \tag{2}$$

The first excited electronic states of the monomers have energies E_A and E_B, respectively. The IR mode has a shifted frequency Ω' in the excited electronic state. The system interacts with the bath/environment, which is modeled to be a collection of harmonic oscillators and the system-bath coupling is approximated to be linear in the position coordinates of the bath

oscillators. The total Hamiltonian is, therefore, given as:

$$H_{g/ex} = \sum_i (E_i + Q_i) \mid i\rangle\langle i \mid + \sum_{i,j;i\neq j} V_{ij} \mid i\rangle\langle j \mid + H_{ph}, \tag{3}$$

where

$$H_{ph} = \sum_{i,k} (\frac{p_{ik}^2}{2m_{ik}} + \frac{1}{2} m_{ik} q_{ik}^2 \omega_{ik}^2). \tag{4}$$

Here, i runs over 3 basis states for H_g, as discussed above and 6 basis states for H_{ex}, respectively. V_{ij} describes the off-diagonal coupling between system states, given by the electronic coupling between the monomers and the vibrational overlap between the nuclear wavefunctions, expressed in terms of the Huang Rhys factors. The system-bath coupling is expressed as $Q_i = \Sigma_k m_{ik} \nu_{ik} q_{ik}$, where m_{ik}, ν_{ik}, q_{ik}, p_{ik} and ω_{ik} are the mass, bath coupling strength, position, momentum and angular frequency, respectively, of the k^{th} bath oscillator pertaining to the i^{th} system state. H_g, when written out, is diagonal with respect to the system basis and therefore, easy to work with. H_{ex}, on the other hand, does not enjoy the same advantage and when diagonalized, can be written as:

$$H_{ex} = \sum_m \varepsilon_m(\mathbf{Q}) \mid m(\mathbf{Q})\rangle\langle m(\mathbf{Q}) \mid + H_{ph}, \tag{5}$$

where $\mid m(\mathbf{Q})\rangle$ is the adiabatic basis. The adiabatic basis is nontrivial to work with, due to its dependence on the system-bath coupling vector, $\mathbf{Q}$. Also, the position coordinates of the bath oscillators do not commute with their momenta. To circumvent this issue, we introduce a unitary transformation $U(\mathbf{Q})$, which maps from the adiabatic basis $\mid m(\mathbf{Q})\rangle$ to the stationary adiabatic basis $\mid m(\mathbf{Q} = \mathbf{0})\rangle$, the adiabatic basis frozen at its equilibrium geometry, to be denoted henceforth as $\mid m\rangle$.[30–32] Thus, $\mid m(\mathbf{Q})\rangle = U(\mathbf{Q}) \mid m\rangle$, where $U(\mathbf{Q})$ is defined as:

$$-i\hbar \nabla_{\mathbf{Q}} U(\mathbf{Q}) = U(\mathbf{Q}) \hat{A}(\mathbf{Q}). \tag{6}$$

Here, $\hat{A}(\mathbf{Q})$ is a vector describing non-adiabatic transitions, with j components, where the

j^{th} component is given as $A^j(\mathbf{Q}) = \sum_{n,m} A^j_{n,m}(\mathbf{Q}) \mid n\rangle\langle m \mid$, where

$$\begin{aligned} A^j_{n,m}(\mathbf{Q}) &= -i\langle n(\mathbf{Q}) \mid \frac{\partial}{\partial Q_j} \mid m(\mathbf{Q})\rangle \\ &= -i\frac{\langle n(\mathbf{Q}) \mid j\rangle\langle j \mid m(\mathbf{Q})\rangle}{\varepsilon_n(\mathbf{Q}) - \varepsilon_m(\mathbf{Q})}. \end{aligned} \tag{7}$$

Therefore, H_{ex}, when unitary transformed, gives $\bar{H}_{ex}$ $(= U^\dagger(\mathbf{Q})H_{ex}U(\mathbf{Q}))$, given as:

$$\bar{H}_{ex} = \bar{H}_0 + \bar{H}_{na}, \tag{8}$$

where $\bar{H}_0 = \sum_m \varepsilon_m(\mathbf{Q}) \mid m\rangle\langle m \mid + H_{ph}$ and $\bar{H}_{na}$ is approximated as:

$$\bar{H}_{na} \approx \frac{1}{2}(P_j A^j(\mathbf{0}) + A^j(\mathbf{0})P_j), \tag{9}$$

where $P_j = \sum_k \nu_{jk} p_{jk}$ and $A^j(\mathbf{0}) = -i\frac{\langle n(\mathbf{0})|j\rangle\langle j|m(\mathbf{0})\rangle}{\varepsilon_n(\mathbf{0})-\varepsilon_m(\mathbf{0})}$. We approximate that the system stays close to its adiabatic limit, so that we can neglect the terms quadratic in $A^j(\mathbf{Q})$ in $\bar{H}_{ex}$, treating non-adiabatic transitions perturbatively. Also, $A^j(\mathbf{Q}) = A^j(\mathbf{0})$, since the overlap between the adiabatic and the site states, and the energy difference between the adiabatic states is mostly insensitive to the phonon fluctuations. While $\varepsilon_m(\mathbf{Q})$ in $\bar{H}_0$ describes fluctuations in a stationary adiabatic state that accounts for decoherence, $\bar{H}_{na}$ describes phonon-mediated population relaxation between the stationary adiabatic states m and n. Therefore, the unitary transformation affords separability of the Hamiltonian into a term responsible for decoherence and a term responsible for incoherent population relaxation, which, in turn, is treated perturbatively. However, it should be noted that as a result of this decoupling, coherence transfer events and coherence to population transfer events are not considered. We do not expect such events to have a significant effect on the current calculations.

We use the intuitive approach of employing Nonlinear Response Functions (NRFs), described by Feynman diagrams, to theoretically evaluate 2DEV spectra. The NRFs for the

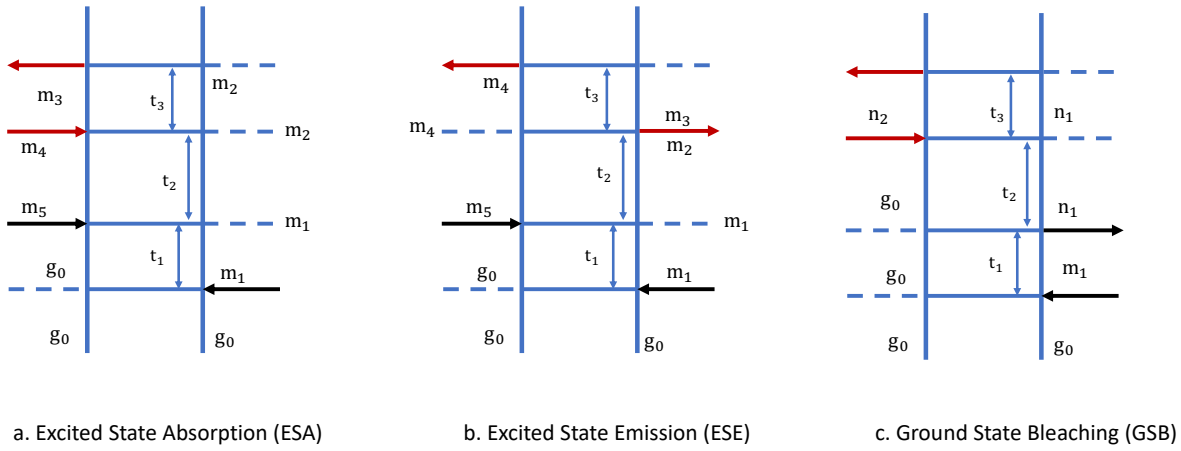

a. Excited State Absorption (ESA) b. Excited State Emission (ESE) c. Ground State Bleaching (GSB)

Figure 1: ESA, ESE and GSB Rephasing Pathways. The black arrows label the electronic pulses and the red arrows label the IR pulses. Here, m_i label the stationary adiabatic states in the electronic excited manifold and n_i label the states in the ground electronic manifold. $n_1 \in \{|\, gv^A_{g0}v^B_{g0}\rangle, |\, gv^A_{g1}v^B_{g1}\rangle\}$ and $n_2 \in \{|\, gv^A_{g0}v^B_{g1}\rangle, |\, gv^A_{g1}v^B_{g0}\}\rangle$. Population relaxation is allowed during the waiting time t_2.

ESA, ESE and GSB pathways are shown in Figure 1. The distinction between the ESA and ESE pathways arises from the fact that in ESA, m_4 undergoes stimulated IR absorption to form m_3, whereas in ESE, m_2 undergoes stimulated IR emission to form m_3. Because of the greater complexity of the energy levels and the re-working of the vibrational oscillator strengths from the mixing, IR stimulated emission becomes possible for transitions that would not exist in uncoupled systems. We do assume that the IR pulse spans the excitonic/vibronic manifold, but not that the visible pulse creates populations in $v = 2$ in the excited manifold. This is seen only for the case of coupled dimers and for systems with more than 2 chromophores/monomers and/or multiple IR modes, where the IR modes could be in their ground or first excited vibrational states. For monomeric systems, the 2DEV spectra are described by the ESA and GSB pathways, provided the initial excitation does not populate $v = 2$ or higher levels. In the GSB pathway shown in Figure 1(c), $n_2 \in \{\mid gv_{g0}^A v_{g1}^B\rangle, \mid gv_{g1}^A v_{g0}^B\}\rangle$, as a result of stimulated IR absorption from g_0. The bandwidth/center wavelength of the visible pulse could be sufficient to create vibrational wavepackets even if the center wavelength was not short enough to do so in the excited state. To describe this, we would need to add Impulsive Stimulated Raman Scattering (ISRS) to our calculations. In Figure 1(c), we consider $n_1 \in \{\mid gv_{g0}^A v_{g0}^B\rangle, \mid gv_{g1}^A v_{g1}^B\rangle\}$, where n_1 is formed by a stimulated electronic emission from m_1. We discuss in detail the ESA rephasing pathway, other pathways are evaluated in an analogous fashion. For easy notation, g_0 denotes the site state $\mid gv_{g0}^A v_{g0}^B\rangle$ and m_i denotes a stationary adiabatic state in the electronic excited manifold, i being a positive integer. It is important to note that the stationary adiabatic states, despite the different technical definition, have the same energies as the eigenstates obtained by diagonalizing $H_{sys,ex}$. The ESA rephasing NRF, depicted pictorially Figure 1(a), is:

$$\mathrm{R_{ESA}}(t_3, t_2, t_1) = \langle \mu_{el}(0)\mu_{vib}(t_1 + t_2 + t_3)\mu_{vib}(t_1 + t_2)\mu_{el}(t_1)\rho(0)\rangle, \tag{10}$$

where $\rho(0) = \mid g_0\rangle\langle g_0 \mid \rho_{ph}(0)$. $\mu_{el/vib}(t)$ is the transition dipole operator in the Heisenberg

representation, defined as $\mu_{el/vib}(t) = e^{iH_{ex}t}\mu_{el/vib}e^{-iH_{ex}t}$. Using these definitions, we have

$$\mathrm{R}_{\mathrm{ESA}}(t_3,t_2,t_1) = \mathrm{Tr}_{ph}\{\langle g_0 \mid \mu_{el}e^{iH_{ex}(t_1+t_2+t_3)}\mu_{vib}e^{-iH_{ex}t_3}\mu_{vib}e^{-iH_{ex}t_2}\mu_{el}e^{-iH_{ex}t_1} \mid g_0\rangle\rho_{ph}(0)\}. \tag{11}$$

We now introduce the unitary transformation and the stationary adiabatic basis.

$$\mathrm{R}_{\mathrm{ESA}}(t_3,t_2,t_1) = \sum_{\{m\}} \mu_{el,g_0m_1}\mu_{vib,m_2m_3}\mu_{vib,m_3m_4}\mu_{el,m_5g_0}e^{-iH_{ph}t_1}\mathrm{F}_{m_1m_2m_3m_4m_5}(t_3,t_2,t_1), \tag{12}$$

where

$$\begin{aligned}\mathrm{F}_{m_1m_2m_3m_4m_5}(t_3,t_2,t_1) = \mathrm{Tr}_{ph}\{&\langle m_1 \mid e^{i\bar{H}_{ex}t_1} \mid m_1\rangle\langle m_1 \mid e^{i\bar{H}_{ex}t_2} \mid m_2\rangle\langle m_2 \mid e^{i\bar{H}_{ex}t_3} \mid m_2\rangle \\ &\times \langle m_3 \mid e^{-i\bar{H}_{ex}t_3} \mid m_3\rangle\langle m_4 \mid e^{-i\bar{H}_{ex}t_2} \mid m_5\rangle\rho_{ph}(0)\}.\end{aligned} \tag{13}$$

In Eq. 13, we have approximated $\langle g_0 \mid \mu \mid m_i(\mathbf{Q})\rangle \approx \langle g_0 \mid \mu \mid m_i\rangle$. In the 2DEV spectroscopy experiments, t_1 and t_3 are small enough compared to phonon relaxation time to neglect phonon-mediated population relaxation. t_2 is the dynamics time. If t_2 is large compared to phonon relaxation time, population relaxation during t_2 needs to be considered. However, if t_2 is small, we can neglect population relaxation during t_2, so that $m_1 = m_2$ and $m_4 = m_5$. Also, since decoherence and population relaxation are essentially different phenomena and mostly independent of each other, we can decouple them at the lowest order. To evaluate $\mathrm{F}_{m_1m_2m_3m_4m_5}(t_3,t_2,t_1)$, we introduce the zeroth order transformed Hamiltonian $\bar{H}_0$ to obtain:

$$\mathrm{F}_{m_1m_2m_3m_4m_5}(t_3,t_2,t_1) \approx \mathrm{D}_{m_1m_2m_3m_4}(t_1,t_2,t_3) \times \mathrm{p}_{m_1m_2m_4m_5}(t_2), \tag{14}$$

where

$$\begin{aligned}\mathrm{D}_{m_1m_2m_3m_4}(t_1,t_2,t_3) = \mathrm{Tr}_{ph}\{&(\hat{T}^\dagger e^{i\int_0^{t_1}dt'\varepsilon_{m_1}(\mathbf{Q}(t'))})(\hat{T}^\dagger e^{i\int_0^{t_2}dt'\varepsilon_{m_2}(\mathbf{Q}(t'))})(\hat{T}^\dagger e^{i\int_0^{t_3}dt'\varepsilon_{m_2}(\mathbf{Q}(t'))}) \\ &\times (\hat{T}e^{-i\int_0^{t_3}dt'\varepsilon_{m_3}(\mathbf{Q}(t'))})(\hat{T}e^{-i\int_0^{t_2}dt'\varepsilon_{m_4}(\mathbf{Q}(t'))})\rho_{ph}(0)\}e^{iH_{ph}t_1},\end{aligned} \tag{15}$$

and

$$\mathrm{p}_{m_1m_2m_4m_5}(t_2) = \mathrm{Tr}_{ph}\{\langle m_1 \mid \mathrm{U}_I^\dagger(t_2) \mid m_2\rangle \rho_{ph}(0) \langle m_4 \mid \mathrm{U}_I(t_2) \mid m_5\rangle\}. \tag{16}$$

In Eq. 15, $\hat{T}^\dagger e^{i\int_0^t dt' \varepsilon_{m_i}(\mathbf{Q}(t'))} = e^{i\varepsilon_{m_i}t}(\hat{T}^\dagger e^{i\int_0^t dt' \nabla_{\mathbf{Q}}\varepsilon_{m_i}(\mathbf{Q}(t'))\cdot\mathbf{Q}(t')})$. The $\mathbf{Q}$ dependence of ε_{m_i} results in decoherence due to the system-phonon coupling. If the environment is modeled by a Debye or Ohmic spectral density, the decoherence term $\mathrm{D}_{m_1m_2m_3m_4}(t_1, t_2, t_3)$ can be evaluated analytically, almost exactly.[30,31] However, for other spectral densities, numerical evaluation is required. $\mathrm{p}_{m_1m_2m_4m_5}(t_2)$ causes population relaxation, where $\mathrm{U}_I = e^{i\bar{H}_0 t}e^{-i\bar{H}_{ex}t}$ and is treated perturbatively by a Markovian master equation, that is evaluated using matrix equations.[30,31] This is justified from the previous approximation that the system resides near its adiabatic limit, so non-adiabatic transitions can be described perturbatively.

In the ESA and ESE rephasing response functions considered together (Figure 1), m_i ($i \in \{1, 2, 3, 4, 5\}$) could be any of the 6 states obtained by diagonalizing $H_{sys,ex}$, resulting in 6^5 pathways. Evaluating contributions for each of these pathways is tedious and time-consuming. Since we are seeking to gain mechanistic insights, we exploit the separability of the transformed Hamiltonian into decoherence and population relaxation. The population relaxation rates are given as:[30]

$$\Gamma_{mn} = 2\pi \frac{1}{e^{\beta\omega_{mn}} - 1} \sum_j J_j(\omega_{mn})(\langle n \mid j\rangle\langle j \mid m\rangle)^2, \tag{17}$$

and $\Gamma_{nm} = e^{\beta\omega_{mn}}\Gamma_{mn}$. Here, m and n label the stationary adiabatic states while j labels the site state. The spectral density for the j^{th} site is given as $J_j(\omega)$ and $\omega_{mn} = \varepsilon_m - \varepsilon_n$, $\omega_{mn} > 0$. The population relaxation rates afford us the flexibility to discard pathways that have negligible rates. In addition, we discard pathways that have small transition dipole moments. Using these two tools, we are able to substantially reduce the number of pathways that have significant contributions to the response function at a given waiting time t_2.

In our calculations, $E_A = 12000\ cm^{-1}$, $E_B = 12900\ cm^{-1}$, $J = 250\ cm^{-1}$, $\sigma = 0.0025$, $\Omega = 1030\ cm^{-1}$ and $\Omega' = 950\ cm^{-1}$. The site states I and IV, in Eq. 2, are electronic-only

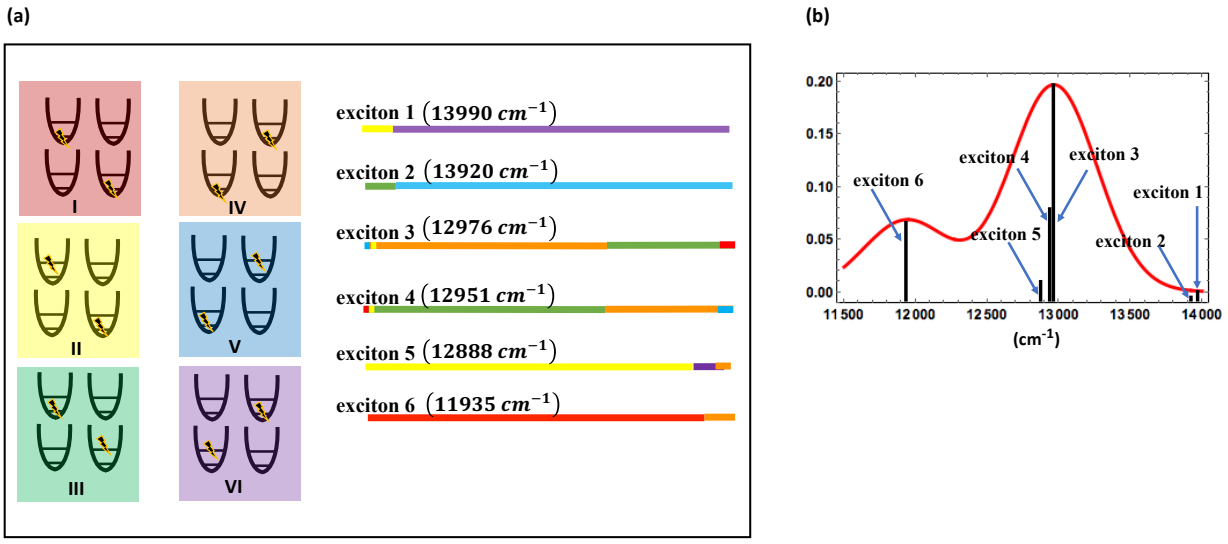

Figure 2: (a) The site basis, labeled by I-VI and the exciton basis, labeled by 1-6. In site I, for example, the left lower potential surface denotes the ground electronic state of A and the left upper potential surface denotes the excited electronic state of A, with the jagged arrows in each surface depicting the state of the vibrational energy. Similarly, the right lower and upper surfaces depict the ground and excited electronic states of B. In the exciton basis, the length of each color bar in each state is representative of the contribution of the corresponding site state. (b) The electronic absorption spectrum of the coupled dimer, with broadening added to mimic an experimental spectrum.

Table 1: IR transition dipole moments

	1	2	3	4	5	6
1			-0.784	-0.602	0.172	
2			-0.772	-0.609	0.159	
3	-0.784	-0.772				0.502
4	-0.602	-0.609				-0.907
5	0.172	0.159				-0.961
6			0.502	-0.907	-0.961	

whereas states II, III, V and VI are vibronic since they have both electronic and vibrational excitations. The electronic transition dipole moments for the transition from the ground to the first excited electronic state for the monomers, A and B, are considered to be unity. The IR transition dipole moments for a vibrational transition from the ground to the first excited vibrational state in each of the monomers, A and B, are also considered to be unity. The eigenvector components and energies for the stationary adiabatic/exciton states, obtained by diagonalizing $H_{sys,ex}$, and electronic transition dipole moments with respect to g_0 are shown in Table SI.1. In the table, we discard very small eigenvectors. Figure 2 shows the site and exciton bases and the electronic absorption spectrum for this coupled dimer. We see that excitons 1, 2 and 6 are formed from either electronic-only or vibronic-only site states, 1 being formed from site states II and VI, 2 from III and V, and 6 from I and IV. Exciton 5 has mostly contributions from the vibronic-only states II and VI, and a smaller contribution from the electronic-only state IV. Excitons 3 and 4 are the most mixed excitons, having sizable contributions from both the electronic-only and vibronic-only site states. Excitons 3, 4 and 6 have large electronic transition dipole moments (-0.961, -0.732 and 0.717, respectively, see Table SI.1). The IR transition dipole moments for the six exciton states are given in Table 1. Excitons 1, 2 and 6 are, each, strongly IR-coupled to excitons 3, 4 and 5. The environment is modeled using the Debye spectral density, with the parameters: electronic reorganization energy $\lambda_{el} = 50\ cm^{-1}$, vibrational reorganization energy $\lambda_{vib} = 5\ cm^{-1}$, cut-off frequency $\omega_c = 53.3\ cm^{-1}$ and temperature $T = 77\ K$. $\alpha_0 = 0.6$ and $\alpha_1 = 1.6$ are the ratio of the displacements for the IR mode in the ground and excited vibrational states in the electronic excited state with respect to the ground electronic state, respectively.[2] The numerical values for the parameters used in our calculation are typical of light-harvesting photosynthetic complexes. The population relaxation rates, calculated using Eq. 17, are given in Table SI.2, where we discard rates that are very small. It is evident that there is strong population relaxation between closely spaced excitons 3 and 4. The visible excitation is assumed to have a bandwidth that spans transitions from g_0 to the excitons 1-6 and the

IR pulse has a bandwidth that covers all intra-exciton transitions.

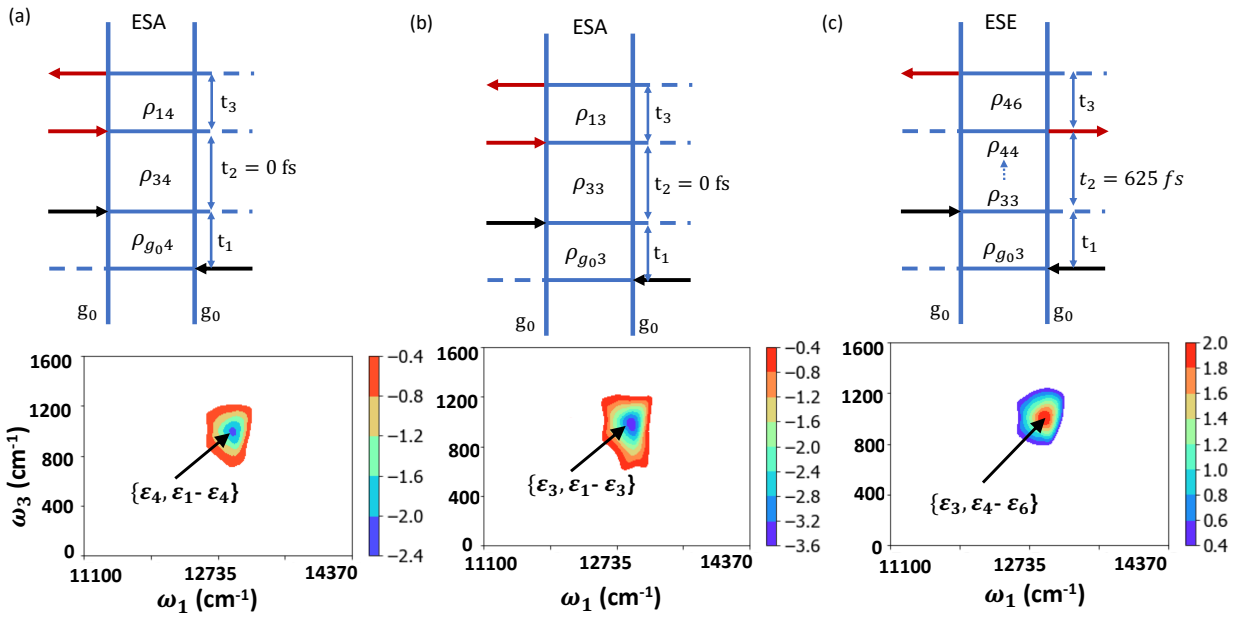

Figure 3: The mapping of a pathway, described by its Feynman diagram, to its 2DEV spectrum. (a) depicts ρ_{34} at $t_2 = 0$ fs, with exciton 3 IR-coupled to exciton 1 in the ESA pathway, which generates a negative peak at $\{\varepsilon_4, \varepsilon_1 - \varepsilon_4\}$, (b) depicts ρ_{33} at $t_2 = 0$ fs, with exciton 3 IR-coupled to exciton 1 in the ESA pathway, which generates a negative peak at $\{\varepsilon_3, \varepsilon_1 - \varepsilon_3\}$ and, (c) depicts $\rho_{33} \rightarrow \rho_{44}$ at $t_2 = 625$ fs, with exciton 4 IR-coupled to exciton 6 in the ESE pathway, which generates a positive peak at $\{\varepsilon_3, \varepsilon_4 - \varepsilon_6\}$.

As discussed above, our method affords us an independent view of coherences and populations. To elucidate this, we depict the components of the 2DEV spectrum describing a coherence at $t_2 = 0$ fs in Fig. 3(a), a population at $t_2 = 0$ fs in 3(b), and a relaxing population at $t_2 = 625$ fs in 3(c), and the mapping to their respective Feynman diagrams. In the plots, ε_i denotes the energy ($\hbar = 1$) of the stationary adiabatic state m_i (see Eq. 15). For the sake of clarity, we describe in detail Fig. 3(a). The initial electronic pulse induces a $g_0 \rightarrow 4$ excitation on the bra side, followed by an electronic excitation $g_0 \rightarrow 3$ after time t_1 on the ket side. During the time interval t_2, we thus have the coherence matrix element ρ_{34} propagating, followed by an IR absorption at time $t_1 + t_2$ on the ket side to exciton 1. Table 1 shows that 3 has a strong IR-coupling to 1, resulting in a strong pres-

ence for this pathway in the 2DEV spectrum at $t_2 = 0$. The system finally emits a signal pulse at $t_1 + t_2 + t_3$, resulting in de-excitation of 1 on the ket side to 4. Therefore, we have $\rho_{g_0 4}$ propagating during t_1, that corresponds to $w_1 = \varepsilon_4 = 12951\ cm^{-1} (\hbar = 1)$, where w_1 is the Fourier transform frequency variable of t_1. ρ_{34} propagates during $t_2 = (0$ fs) and ρ_{14} propagates during t_3, resulting in $w_3 = \varepsilon_1 - \varepsilon_4 = 1039\ cm^{-1}$, where w_3 is the Fourier transform frequency variable of t_3. Comparing with Figure 1(a), it is easy to deduce that for the NRF calculation, $m_1 = m_2 = 4$, $m_3 = 1$ and $m_4 = m_5 = 3$. Similarly, in Figure 3(b), $\rho_{g_0 3}$ propagates during t_1, resulting in $w_1 = \varepsilon_3 = 12976\ cm^{-1}$. The population density matrix element ρ_{33} propagates during $t_2 = 0$ fs and ρ_{13} propagates during t_3, resulting in $w_3 = \varepsilon_1 - \varepsilon_3 = 1014\ cm^{-1}$. For this pathway, $m_1 = m_2 = 3$, $m_3 = 1$ and $m_4 = m_5 = 3$. In Figure 3(c), $\rho_{g_0 3}$ propagates during t_1, resulting in $w_1 = \varepsilon_3 = 12976\ cm^{-1}$, the population density matrix element ρ_{33} undergoes downhill population relaxation during $t_2 (= 625$ fs) to ρ_{44}. From Table 1, 4 is strongly IR-coupled to 6. However, $\varepsilon_6 < \varepsilon_4$, so we have a stimulated emission on the bra side inducing this transition. Thus, ρ_{46} propagates during t_3, resulting in $w_3 = \varepsilon_4 - \varepsilon_6 = 1016\ cm^{-1}$. In 3(a) and (b), since the IR pulse causes a transition to a higher energy state (stimulated absorption), we have the ESA pathway for these cases, resulting in negative peaks. On the other hand, in 3(c), the IR pulse de-excites to a lower energy state (stimulated emission), hence we have the ESE pathway, resulting in a positive peak. Therefore, we find that not all excited state signals are negative for a strongly coupled dimer, in contrast to the weak coupling case where it is possible to arrange pulse durations and center wavelengths so that only negative ESA peaks are observed.

Excitons 3, 4 and 6 have large values of electronic transition dipole moments. Excitons 3 and 4 are, in turn, strongly IR-coupled to excitons 1, 2 and 6, and exciton 6 is strongly IR-coupled to 4 and 5, resulting in large initial populations from these pathways. In Figure 4, (a), (b), (c) and (d) show some of the important population contributions at $t_2 = 0$ fs: (a) ρ_{33}, exciton 3 being IR-coupled to exciton 2, (b) ρ_{44}, exciton 4 being IR-coupled to exciton 6, (c) ρ_{66}, exciton 6 being IR-coupled to exciton 4, and (d) ρ_{66}, exciton 6 being IR-coupled to

exciton 5. The peaks from ρ_{66} propagating during t_2 are negative, since the IR pulse induces a stimulated absorption from 6 to 4 or 5. On the other hand, for ρ_{33} and ρ_{44} propagating during t_2, we have negative ESA peaks if they undergo absorption to exciton 1 or 2 and a positive ESE peak if the IR pulse induces a stimulated emission to exciton 6. Phonon-mediated population relaxation is strongest between the strongly mixed excitons 3 and 4 (see Table SI.2, for the population relaxation rates). We are able to evaluate contributions from the important pathways that contribute to population relaxation at $t_2 = 625$ fs. We show one such instance in Figure 3(c) where population relaxes from 3 to 4, with 4 being strongly IR-coupled to 6, resulting in a positive ESE peak.

Figures 4 (e) and (f) show some of the most prominent coherences at $t_2 = 0$ fs. The coherences between the strongly mixed excitons, 3 and 4, are the strongest and of similar magnitudes to the initial populations at 3, 4 and 6 (see Table SI.3). Table 1 shows that excitons 3 and 4 are each strongly IR-coupled to excitons 1, 2 and 6, hence the related pathways are the most important. Thus, if the IR pulse excites 3 or 4 to the higher energy states 1 or 2, we have negative peaks arising due to the ESA pathway whereas if the IR pulse induces a stimulated emission from 3 or 4 to the lower energy exciton 6, we have negative peaks arising from the relevant ESE contribution. Figure 4 (e) shows ρ_{34} at $t_2 = 0$, with exciton 3 being IR-coupled to exciton 1. Figure 4 (f) shows ρ_{43} at $t_2 = 0$, with exciton 3 being IR-coupled to exciton 6. The coherences arising from the other excitons do not have a strong presence, even at $t_2 = 0$. Figures 4 (g) and (h) show the evolution of the 2DEV amplitudes of the coherences shown in Figures 4 (e) and (f), respectively, with t_2. They decay by ~ 200 fs. The vibronic decoherence, here, is thus much more rapid than a vibrational coherence in the ground electronic state, which has a typical decoherence timescale of several picoseconds. The decoherence time is expected to be longer for stronger electronic coupling between the monomers and larger Huang-Rhys parameters, as these lead to more strongly-mixed excitons. On the other hand, increasing the environmental reorganization energy, specifically the electronic reorganization energy, will result in a shorter decoherence time.

No obvious oscillatory character is evident in the coherence peaks as a result of the rapid decoherence, and the low frequency of the 3, 4 beat.

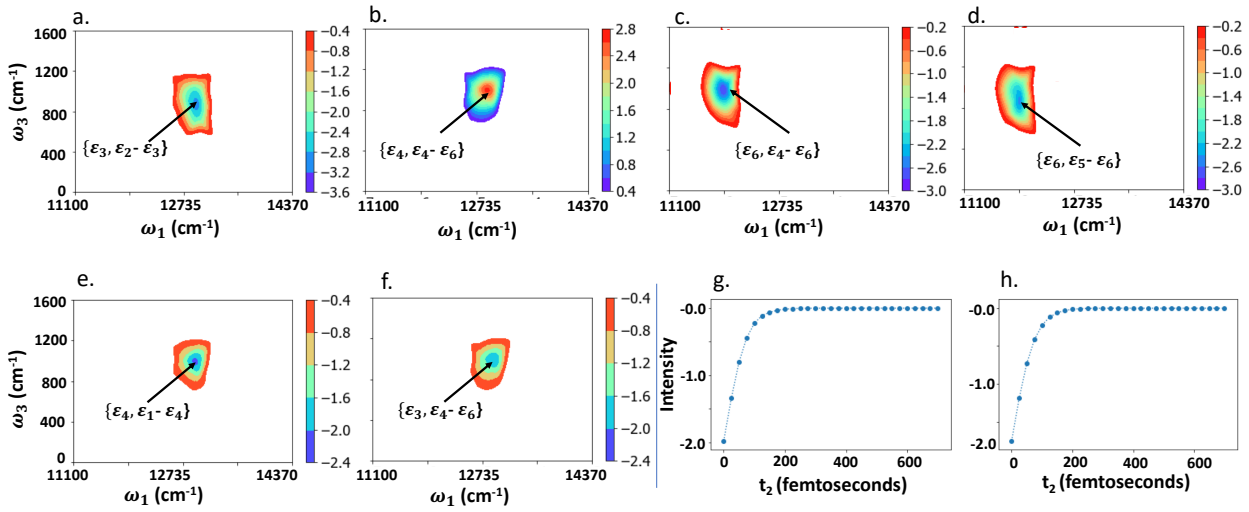

Figure 4: Contributions to 2DEV spectra from populations and coherences at $t_2 = 0$. (a) ρ_{33} (population), exciton 3 IR-coupled to exciton 2, at $t_2 = 0$; ESA pathway; $w_1 = \varepsilon_3 = 12976\ cm^{-1}$ and $w_3 = \varepsilon_2 - \varepsilon_3 = 944\ cm^{-1}$, (b) ρ_{44} (population), exciton 4 IR-coupled to exciton 6, at $t_2 = 0$; ESE pathway; $w_1 = \varepsilon_4 = 12951\ cm^{-1}$ and $w_3 = \varepsilon_4 - \varepsilon_6 = 1016\ cm^{-1}$, (c) ρ_{66} (population), exciton 6 IR-coupled to exciton 4, at $t_2 = 0$; ESA pathway; $w_1 = \varepsilon_6 = 11935\ cm^{-1}$ and $w_3 = \varepsilon_4 - \varepsilon_6 = 1016\ cm^{-1}$, (d) ρ_{66} (population), exciton 6 IR-coupled to exciton 5, at $t_2 = 0$; ESA pathway; $w_1 = \varepsilon_6 = 11935\ cm^{-1}$ and $w_3 = \varepsilon_5 - \varepsilon_6 = 953\ cm^{-1}$, (e) ρ_{34} (coherence), exciton 3 IR-coupled to exciton 1, at $t_2 = 0$; ESA pathway; $w_1 = \varepsilon_4 = 12951\ cm^{-1}$ and $w_3 = \varepsilon_1 - \varepsilon_4 = 1039\ cm^{-1}$, (f) ρ_{43} (coherence), exciton 3 IR-coupled to exciton 6, at $t_2 = 0$; ESE pathway; $w_1 = \varepsilon_3 = 12976\ cm^{-1}$ and $w_3 = \varepsilon_4 - \varepsilon_6 = 1016\ cm^{-1}$, (g) coherence ρ_{34}, with exciton 3 IR-coupled to exciton 1, evolving with t_2 and (h) coherence ρ_{43}, with exciton 3 IR-coupled to exciton 6, evolving with t_2. We see from (g) and (h) that the coherences decay off by 200 fs.

Figure 5 shows the total 2DEV spectra, the sum of the ESA, ESE and GSB pathways, at $t_2 = 0$ fs and $t_2 = 625$ fs, respectively. The GSB pathway has positive peaks emerging due to excitons 3, 4 and 6, owing to their large electronic transition dipole moments. For ESA and ESE pathways, at $t_2 = 0$, the spectrum shows the contributions from large initial populations at excitons 3, 4 and 6, and large initial coherences between 3 and 4. In Fig. 5(a), A and C contain concentrated positive peaks with underlying more diffuse negative peaks (as evident from the diffuse tails seen in B and D) resulting in cancellation of some intensities at A and C. The chief components contributing to these peaks are shown in Table SI.3.

At $t_2 = 625$ fs, the positive peaks have higher intensities compared to $t_2 = 0$ peaks. This arises chiefly from the vanishing negative peaks at $t_2 = 625$ fs originating from the coherence density matrix elements ρ_{34} and ρ_{43}, propagating during t_2 and each being IR-coupled to 1, 2 and 6, respectively, due to rapid decoherence. The chief components contributing to the peaks at E and F in Fig. 5(b) are shown in Table SI.4.

To conclude, for this coupled dimeric system, where we have strongly mixed excitons 3 and 4, the initial coherences between these excitons are similar in magnitude to the initial populations from excitons 3, 4 and the electronic-only lowest energy exciton 6. The initial populations are dictated by the electronic transition dipole moments of the excitons and the peak intensities are determined by both the initial electronic dipole moments and the IR transition dipole moments. Population relaxation is the strongest between the strongly mixed excitons 3 and 4. Decoherence occurs rapidly, resulting in more positive intensities in the 2DEV spectrum with increasing t_2, until decoherence is complete. The positive peaks arise from the GSB and the ESE population pathways. The ESE pathways for the coherences ρ_{34} and ρ_{43} during t_2, and IR-coupled to 6, are seen to have negative peaks due to the negative initial amplitude and with increasing t_2, decay to zero due to rapid decoherence. The ESA pathway leads to negative peaks, for both populations and the ρ_{43} and ρ_{34} coherences, propagating during t_2, and IR-coupled to 1 and 2, before the peaks decay to zero.

The calculations above demonstrate that the interpretation of 2DEV spectra of vibronically coupled systems is considerably more complex than in weakly coupled systems that have an IR mode that is non-resonant with the energy gap between the electronic excitons formed by the monomers. Nonetheless, the richness of the spectra, the presence of short-lived features arising from vibronic coherences and the necessity to take both visible and infrared transition moments into account suggest that careful comparison with experimental data will enable the role of vibronic effects in ultrafast reactions to be clarified. Several developments of the model described above are likely to be significant in developing the necessary machinery for such a program. First, anisotropy measurements will aid assignments. Second, as

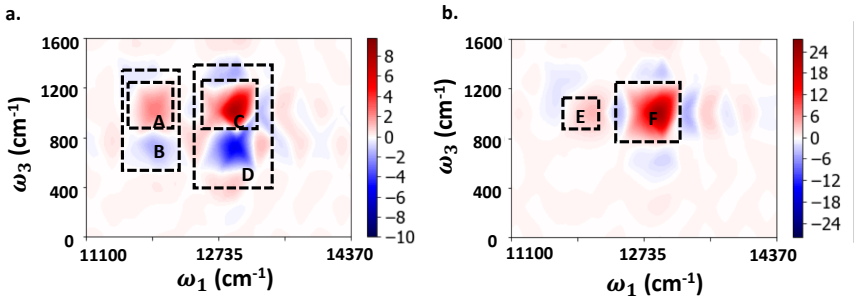

Figure 5: 2DEV spectra at (a) $t_2 = 0$ fs and (b) $t_2 = 625$ fs. The chief components contributing to the intensities at A, B, C, D, E and F are discussed in Table SI.3 and Table SI.4.

the coherences are sensitive to the degree of resonance between donor and acceptor levels, the role of inhomogeneous broadening of both electronic and vibrational levels needs to be carefully considered. It is also noteworthy that weak transitions that may not be evident in a 1D or a 2D electronic spectrum can be easily observed in a 2DEV spectrum through the IR transition moments.

The role of resonant vibrations on population relaxation is also significant. As we show in a forthcoming publication, when there are no resonances between the vibrational modes and the electronic eigenstates, population relaxation between electronic-only eigenstates is slower than that between the vibronically mixed excitons when resonance is present. The ability to separate the contributions from coherence and population relaxation is a feature of the near-analytical method developed here. Whether such discrimination can be achieved in 2DEV spectroscopy constitutes a challenge to experimentalists, but in any case the specificity of the initial states and coherences, along with the relaxation pathways, suggest that 2DEV spectroscopy will be of significant value in the characterization of complex vibronic systems, such as photosynthetic pigment-protein complexes.

Finally we note that while specific peak frequencies and amplitudes are, of course, controlled by the parameters of our model, we expect the overall behavior of the 2DEV spectrum

to be generic for strongly coupled vibronic systems. In future work, we will explore the roles of multiple vibrational degrees of freedom, the nature of the spectral lineshapes, how well singular value decomposition works to recover underlying dynamics, and what tests might be available to discriminate between vibronic coherences and short-lived populations.

Acknowledgments

This work was supported by the U.S. Department of Energy, Office of Science, Basic Energy Sciences, Chemical Sciences, Geosciences, and Biosciences Division under Field Work Proposal 449A. This research used resources of the National Energy Research Scientific Computing Center (NERSC), a U.S. Department of Energy Office of Science User Facility operated under Contract No. DE-AC02-05CH11231. We thank Eric Arsenault for helpful discussions.

Supporting Information

Table SI.1: Eigenvectors, eigenstate energies and electronic transition dipole moments of the excitons, Table SI.2: population relaxation rates, Table SI.3: chief components of the 2DEV spectrum at $t_2 = 0$ fs, Table SI.4: chief components of the 2DEV spectrum at $t_2 = 625$ fs.

References

(1) Lewis, N. H. C.; Dong, H.; Oliver, T. A. A.; Fleming, G. R. A method for the direct measurement of electronic site populations in a molecular aggregate using two-dimensional electronic-vibrational spectroscopy. *The Journal of Chemical Physics* **2015**, *143*, 124203.

(2) Lewis, N. H. C.; Dong, H.; Oliver, T. A. A.; Fleming, G. R. Measuring correlated electronic and vibrational spectral dynamics using line shapes in two-dimensional

electronic-vibrational spectroscopy. *The Journal of Chemical Physics* **2015**, *142*, 174202.

(3) Dong, H.; Lewis, N. H. C.; Oliver, T. A. A.; Fleming, G. R. Determining the static electronic and vibrational energy correlations via two-dimensional electronic-vibrational spectroscopy. *The Journal of Chemical Physics* **2015**, *142*, 174201.

(4) Lewis, N. H. C.; Fleming, G. R. Two-Dimensional Electronic-Vibrational Spectroscopy of Chlorophyll a and b. *The Journal of Physical Chemistry Letters* **2016**, *7*, 831–837, PMID: 26894783.

(5) Lewis, N. H. C.; Gruenke, N. L.; Oliver, T. A. A.; Ballottari, M.; Bassi, R.; Fleming, G. R. Observation of Electronic Excitation Transfer Through Light Harvesting Complex II Using Two-Dimensional Electronic–Vibrational Spectroscopy. *The Journal of Physical Chemistry Letters* **2016**, *7*, 4197–4206.

(6) Gaynor, J. D.; Petrone, A.; Li, X.; Khalil, M. Mapping Vibronic Couplings in a Solar Cell Dye with Polarization-Selective Two-Dimensional Electronic–Vibrational Spectroscopy. *The Journal of Physical Chemistry Letters* **2018**, *9*, 6289–6295.

(7) Gaynor, J. D.; Khalil, M. Signatures of vibronic coupling in two-dimensional electronic-vibrational and vibrational-electronic spectroscopies. *The Journal of Chemical Physics* **2017**, *147*, 094202.

(8) Hybl, J. D.; Albrecht, A. W.; Faeder, S. M. G.; Jonas, D. M. Two-dimensional electronic spectroscopy. *Chemical Physics Letters* **1998**, *297*, 307 – 313.

(9) Mukamel, S. Multidimensional Femtosecond Correlation Spectroscopies of Electronic and Vibrational Excitations. *Annual Review of Physical Chemistry* **2000**, *51*, 691–729, PMID: 11031297.

(10) Zigmantas, D.; Read, E. L.; Mančal, T.; Brixner, T.; Gardiner, A. T.; Cogdell, R. J.; Fleming, G. R. Two-dimensional electronic spectroscopy of the B800–B820 light-harvesting complex. *Proceedings of the National Academy of Sciences* **2006**, *103*, 12672–12677.

(11) Noda, I. Two-dimensional infrared spectroscopy. *Journal of the American Chemical Society* **1989**, *111*, 8116–8118.

(12) Zanni, M. T.; Hochstrasser, R. M. Two-dimensional infrared spectroscopy: a promising new method for the time resolution of structures. *Current Opinion in Structural Biology* **2001**, *11*, 516 – 522.

(13) Woutersen, S.; Hamm, P. Nonlinear two-dimensional vibrational spectroscopy of peptides. *Journal of Physics: Condensed Matter* **2002**, *14*, R1035.

(14) Panitchayangkoon, G.; Hayes, D.; Fransted, K. A.; Caram, J. R.; Harel, E.; Wen, J.; Blankenship, R. E.; Engel, G. S. Long-lived quantum coherence in photosynthetic complexes at physiological temperature. *Proceedings of the National Academy of Sciences* **2010**, *107*, 12766–12770.

(15) Engel, G. S.; Calhoun, T. R.; Read, E. L.; Ahn, T.-K.; Mančal, T.; Cheng, Y.-C.; Blankenship, R. E.; Fleming, G. R. Evidence for wavelike energy transfer through quantum coherence in photosynthetic systems. *Nature* **2007**, *446*, 782.

(16) Lee, H.; Cheng, Y.-C.; Fleming, G. R. Coherence Dynamics in Photosynthesis: Protein Protection of Excitonic Coherence. *Science* **2007**, *316*, 1462–1465.

(17) Tiwari, V.; Peters, W. K.; Jonas, D. M. Electronic resonance with anticorrelated pigment vibrations drives photosynthetic energy transfer outside the adiabatic framework. *Proceedings of the National Academy of Sciences* **2013**, *110*, 1203–1208.

(18) Chin, A. W.; Prior, J.; Rosenbach, R.; Caycedo-Soler, F.; Huelga, S. F.; Plenio, M. B. The role of non-equilibrium vibrational structures in electronic coherence and recoherence in pigment–protein complexes. *Nature Physics* **2013**, *9*, 113.

(19) Lim, J.; Paleček, D.; Caycedo-Soler, F.; Lincoln, C. N.; Prior, J.; von Berlepsch, H.; Huelga, S. F.; Plenio, M. B.; Zigmantas, D.; Hauer, J. Vibronic origin of long-lived coherence in an artificial molecular light harvester. *Nature Communications* **2015**, *6*, 7755.

(20) Halpin, A.; Johnson, P. J. M.; Tempelaar, R.; Murphy, R. S.; Knoester, J.; Jansen, T. L. C.; Miller, R. J. D. Two-dimensional spectroscopy of a molecular dimer unveils the effects of vibronic coupling on exciton coherences. *Nature Chemistry* **2014**, *6*, 196.

(21) Chenu, A.; Christensson, N.; Kauffmann, H. F.; Mančal, T. Enhancement of Vibronic and Ground-State Vibrational Coherences in 2D Spectra of Photosynthetic Complexes. *Scientific Reports* **2013**, *3*, 2029.

(22) Christensson, N.; Kauffmann, H. F.; Pullerits, T.; Mančal, T. Origin of Long-Lived Coherences in Light-Harvesting Complexes. *The Journal of Physical Chemistry B* **2012**, *116*, 7449–7454, PMID: 22642682.

(23) Yeh, S.-H.; Hoehn, R. D.; Allodi, M. A.; Engel, G. S.; Kais, S. Elucidation of near-resonance vibronic coherence lifetimes by nonadiabatic electronic-vibrational state character mixing. *Proceedings of the National Academy of Sciences* **2018**,

(24) Stones, R.; Olaya-Castro, A. Vibronic Coupling as a Design Principle to Optimize Photosynthetic Energy Transfer. *Chem* **2016**, *1*, 822 – 824.

(25) Dijkstra, A. G.; Wang, C.; Cao, J.; Fleming, G. R. Coherent Exciton Dynamics in the Presence of Underdamped Vibrations. *The Journal of Physical Chemistry Letters* **2015**, *6*, 627–632, PMID: 26262477.

(26) Fujihashi, Y.; Higashi, M.; Ishizaki, A. Intramolecular Vibrations Complement the Robustness of Primary Charge Separation in a Dimer Model of the Photosystem II Reaction Center. *The Journal of Physical Chemistry Letters* **2018**, *9*, 4921–4929.

(27) Bennett, D. I. G.; Malý, P.; Kreisbeck, C.; van Grondelle, R.; Aspuru-Guzik, A. Mechanistic Regimes of Vibronic Transport in a Heterodimer and the Design Principle of Incoherent Vibronic Transport in Phycobiliproteins. *The Journal of Physical Chemistry Letters* **2018**, *9*, 2665–2670, PMID: 29683676.

(28) Tiwari, V.; Peters, W. K.; Jonas, D. M. Electronic energy transfer through non-adiabatic vibrational-electronic resonance. I. Theory for a dimer. *The Journal of Chemical Physics* **2017**, *147*, 154308.

(29) Fujihashi, Y.; Fleming, G. R.; Ishizaki, A. Impact of environmentally induced fluctuations on quantum mechanically mixed electronic and vibrational pigment states in photosynthetic energy transfer and 2D electronic spectra. *The Journal of Chemical Physics* **2015**, *142*, 212403.

(30) Bhattacharyya, P.; Sebastian, K. L. Adiabatic eigenfunction-based approach for coherent excitation transfer: An almost analytical treatment of the Fenna-Matthews-Olson complex. *Phys. Rev. E* **2013**, *87*, 062712.

(31) Bhattacharyya, P.; Sebastian, K. L. Adiabatic Eigenfunction Based Approach to Coherent Transfer: Application to the Fenna–Matthews–Olson (FMO) Complex and the Role of Correlations in the Efficiency of Energy Transfer. *The Journal of Physical Chemistry A* **2013**, *117*, 8806–8813, PMID: 23805909.

(32) Bhattacharyya, P.; Ananth, N. An Almost Analytical Approach to Simulating 2D Electronic Spectra. *arXiv:1705.00738*